# A modal sensor integrated circular cylindrical wedge wave ultrasonic motor

Tai-Ho Yu, Ching-Chung Yin*

*Department of Mechanical Engineering, National Chiao Tung University, 1001 Ta Hsueh Road, Hsinchu 30010, Taiwan, Republic of China*

## ABSTRACT

This study investigates a new circular cylindrical wedge wave ultrasonic motor (WW-USM) integrated with modal sensors. The presented motor is driven by continuous wedge waves of the fundamental modes with an integer circumferential number. In this design, the constructive interference of two equal-intensity standing waves actuated by two comb transducers generates a traveling wedge wave. Dual-phase electrodes were parallel to the axis placed on a piezoelectric (PZT) tube at a distance of 1/4 wavelength. Two orthogonal sinusoidal signals at the resonant frequency of designated flexural mode exerting on the electrodes have the WW-USM operate in bidirectional rotation. The base height of the stator was appropriately tuned to achieve an excellent modal separation from other vibration modes. A modal sensor on the border of the PZT tube was designed to detect the dynamic characteristics of the WW-USM and to improve the performance. The wedge wave motor has a flexible mechanical performance between the angular speed and output torque. Varying the contact position of the rotor on the inclined surface of the stator may exchange the angular speed for torque output. No further modification of the entire motor structure is needed. The prototype WW-USM driven by the flexural mode $F(1, 4)$ under 1 N static preload was operated by an AC voltage of $400\,V_{pp}$ at the frequency of 36.605 kHz. The maximum values of angular speed, output torque, and electromechanical transduction efficiency are 225 rpm, 15.736 mN m, and 16.22%, respectively.

© 2011 Elsevier B.V. All rights reserved.

## 1. Introduction

The ultrasonic motor (USM) is driven by the piezoelectric actuator induced mechanical vibrations or traveling waves around the stator via frictional force acting on the contact surfaces between stator and rotor. Featuring simpler structure, higher torque at low revolution speed, more freedom from electromagnetic interference, and better controllability, the USM outperforms traditional electro-magnetic motors in some application areas. Researchers have developed various USMs over the past four decades. Different kinds of shapes have been considered for the geometries of ultrasonic piezoelectric motors, including disk, ring, solid cylinder, hollow cylinder, and so on.

Sashida [1] pioneered the fabrication of a ring-type traveling wave USM in 1982. Many subsequent researches continuously extended his achievement. In 1991, Kurosawa and Ueha [2] developed a hybrid cylindrical USM, in which the stator consisted of a torsional vibrator and longitudinal vibrator. Hagedorn and Wallaschek [3,4] presented a mathematical description of the disk-type traveling wave USM stator in 1992. They calculated the transverse forced vibration of thin annular plates using a finite difference scheme. Aoyagi et al. [5] dealt with the USMs in which longitudinal

and bending multi-modes were used to drive a rectangular plate vibrator in 1992. Morita et al. [6] devised a cylindrical micro USM in 1998, in which a lead zirconate titanate thin film was deposited on a titanium substrate by a single process hydrothermal method. Lu et al. [7] reported a contact interface model with projections on the surface of the rotor of a traveling wave USM in 2001. In 2002, Koc et al. [8] designed a hollow cylindrical USM excited by two beam modes in orthogonal planes. Sun et al. [9] developed a new analytical model for traveling wave USM and experimentally verified the correctness. Xu et al. [10] presented a mechanical model of a longitudinal oscillation USM and a method to analyze its frequency–temperature attributes in 2003. Tominaga et al. [11] developed a ridge-mode traveling wave linear USM in 2005. Vyshnevskyy et al. [12] proposed a piezoelectric hollow cylinder USM coupled the tangential-axial resonant modes in 2005. Iula and Pappalardo [13] developed a high-power traveling wave USM by use of Langeven transducers to excite the mode (0, 5) traveling wave on a thin steel ring in 2006. Ma et al. [14] devised a two-phase traveling wave USM using multiple piezoelectric tubes in 2009. Sun et al. [15] designed a piezoelectric linear USM having the circular cylindrical stator and slider in 2010. Many circular cylindrical USMs are driven by beam mode resonators, and have a higher mechanical output power than other type motors. In the beam mode drive cylindrical USM, the cross section remains circular and the cylinder deflects in a manner similar to an elastic beam. The rotor contacts the friction surface of the resonator at only one point

---

* Corresponding author.
  *E-mail address:* ccyin@faculty.nctu.edu.tw (C.-C. Yin).

around the circumference. Consequently, the motor experiences uneven rotation and stress concentration. Increasing the contact points between the circular stator and a rotor around the circumference helps prevent wobbling and failure during operation.

Lagasse [16] discovered acoustic wedge waves in 1972. It was found that most of the elastic energy carried by wedge waves is confined within a region of approximately one wavelength near the apex of a wedge. In spite of no exact solution, Krylov [17,18] developed the approximations for phase velocities of wedge waves propagating in linear and circular wedges in 1990 and 1999. Hladky-Hennion [19] conducted a finite element analysis on acoustic wave propagation in the wedge-like waveguides in 1996. Krylov [20] proposed a novel method for submarine propulsion by guided flexural waves around the edge of the attached elastic fins in 1994. Later, Krylov and Pritchard [21,22] experimentally verified the feasibility. Using acoustic waveguides as stators is a trend in recent USM designs [11,13,23,24]. Acoustic guided waves can propagate far with less energy dissipation because particles resonantly oscillate in cross-section of the elastic waveguides. The resonant flexural modes around a circular wedge represent the standing wedge waves which have integer circumferential number.

This study presents the working principle of the WW-USM and a promising design method for the desired resonator. Simulation results indicate that an appropriate upper base height yields a satisfactory modal separation near the designated resonant mode. This work investigated the dynamic characteristics of the motor by detecting the impedance curve and the quality of traveling waves using modal sensors around the stator. The performance of a prototype four-wavelength WW-USM was evaluated in accordance with the measured T–N curves. Experimental results reveal that the trade-off between fast angular speed and high torque essentially depends on the contact position at which the rotor touches the stator. It demonstrates that the proposed motor has a flexible mechanical output without a need to modify the entire WW-USM structure.

## 2. Basic principles

### 2.1. Frequency equation

It was reported in our earlier work [24] that the resonant vibration modes and phase velocities of flexural waves circumferentially propagating in circular wedges could be efficiently evaluated using a bi-dimensional finite element method. This study used a commercial finite element code ANSYS 10.0 (ANSYS Inc., Canonsburg, PA, USA) for numerical calculations. The eight-node coupled-field hexahedral element SOLID5 was adopted to model the stator. Fig. 1 shows an exploded view of the WW-USM and the designated resonant mode $F(1, 4)$ together with a polar coordinate system ($r$, $\theta$, $z$). The elastic displacement vector **u** and electric potential $\varphi$ at any point inside each element can be interpolated by nodal displacement vector **d** and nodal electric potential $\mathbf{\Phi}$ in the form

$$\left\{ \begin{array}{c} \mathbf{u} \\ \varphi \end{array} \right\} = \left\{ \begin{array}{c} u_r(r, \theta, z) \\ u_z(r, \theta, z) \\ u_\theta(r, \theta, z) \\ \varphi(r, \theta, z) \end{array} \right\} = \left\{ \begin{array}{c} \mathbf{N}_u \mathbf{d} \\ \mathbf{N}_\phi \mathbf{\Phi} \end{array} \right\} \tag{1}$$

The time dependence $e^{-j\omega t}$ in all field variables is suppressed throughout. The matrices $\mathbf{N}_u$, $\mathbf{N}_\phi$ are interpolation functions in conjunction with each nodal displacement and electric potential. Based
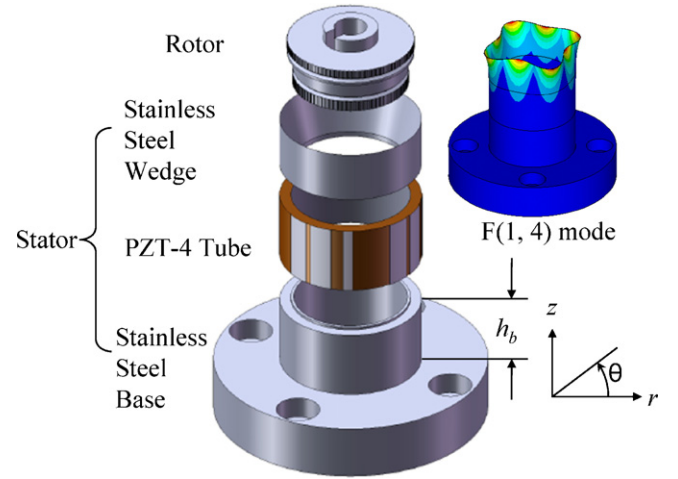


**Fig. 1.** Exploded view of the WW-USM and its resonant flexural mode $F(1, 4)$.

on Hamilton's principle, a system of equations for wedge waves traveling along the circular cylindrical stator are derived as

$$\begin{bmatrix} \mathbf{M} & 0 \\ 0 & 0 \end{bmatrix} \left\{ \begin{array}{c} \ddot{\mathbf{d}} \\ \ddot{\Phi} \end{array} \right\} + \begin{bmatrix} \mathbf{K}_{uu} & \mathbf{K}_{u\phi} \\ \mathbf{K}_{\phi u} & \mathbf{K}_{\phi\phi} \end{bmatrix} \left\{ \begin{array}{c} \mathbf{d} \\ \Phi \end{array} \right\} = \left\{ \begin{array}{c} 0 \\ 0 \end{array} \right\} \tag{2}$$

where $\mathbf{M}$, $\mathbf{K}_{uu}$, $\mathbf{K}_{u\phi}$, $\mathbf{K}_{\phi\phi}$ denote the global mass matrix as well as the global elastic, elasto-piezoelectric, and piezoelectric stiffness matrices, respectively. The existence of nontrivial solution to Eq. (2) yields the frequency equation,

$$\det \left( \begin{bmatrix} \mathbf{K}_{uu} & \mathbf{K}_{u\phi} \\ \mathbf{K}_{\phi u} & \mathbf{K}_{\phi\phi} \end{bmatrix} - \omega^2 \begin{bmatrix} \mathbf{M} & 0 \\ 0 & 0 \end{bmatrix} \right) = 0 \tag{3}$$

The resonant flexural modes can be calculated by standard numerical scheme after determining the angular frequency $\omega = 2\pi f$ in Eq. (3).

### 2.2. Dual-phase drive principle

Two sets of comb transducers parallel to the axis placed on the outer PZT tube are used to excite two standing waves. The amplitude of particle motion is substantially a function of the circumferential position. The constructive interference of two equal-intensity standing waves with a 90° phase difference forms a traveling wave. Both comb electrodes have a stripe width equal to one quarter of the wavelength.

Two sets of dual-phase transducers are sketched in Fig. 2. Suppose that the displacement fields induced by transducers A and B are of the same amplitude. Both are expressed to be the sum of two waves traveling in opposite direction in the form

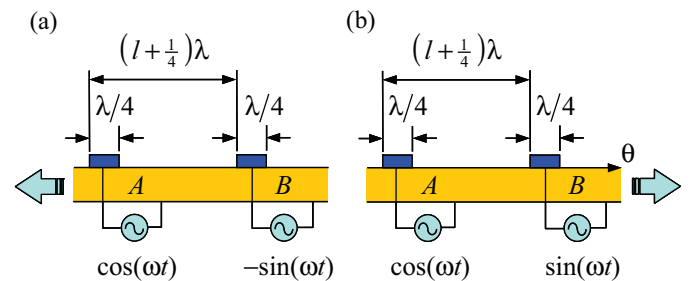$$u_A = e^{i(n\theta - \omega t)} + e^{i(n\theta + \omega t)} \tag{4}$$



**Fig. 2.** Dual-phase electrode placement for generating a constructive wave traveling toward (a) negative $\theta$ and (b) positive $\theta$ direction.
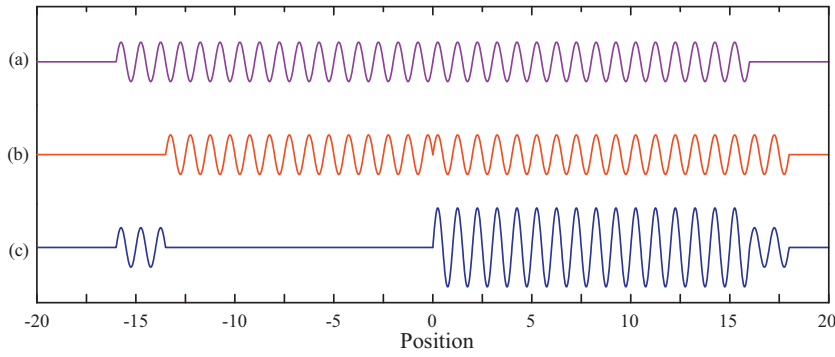
**Fig. 3.** Constructive and destructive interferences of two wave motions (a) $u_A$, (b) $u_B$, and (c) $u_A + u_B$.

$$u_B = e^{i[n(\theta-\xi)-\omega(t-\tau)]} + e^{i[n(\theta-\xi)+\omega(t-\tau)]} \qquad (5)$$

where $\tau$ indicates the time delay or phase difference between the time-harmonic voltages exerted on transducers A and B; $\xi$ is the circumferential space interval between transducers A and B; the integer $n$ denotes the circumference number.

The sufficient condition for the constructive interference traveling toward positive $\theta$ direction can be given by

$$\xi = \left(l + \frac{1}{4}\right)\lambda, \quad \tau = \frac{T}{4} \qquad (6)$$

where $l$ is a positive integer, $T$ is the period, and $\lambda$ is the circumferential wavelength.

Similarly, the sufficient condition for the same configuration to generate a constructive interference propagating toward negative $\theta$ direction is

$$\xi = \left(l + \frac{1}{4}\right)\lambda, \quad \tau = -\frac{T}{4} \qquad (7)$$

According to both conditions described in Eqs. (6) and (7), we placed two sets of electrodes with a space interval of $(l+1/4)\lambda$ on the circumference of piezoelectric tube and exerted two sinusoidal signals with a phase difference of $T/4$ on the electrodes. As shown in Fig. 3, a constructive interference formed by a combination of two equal amplitude sinusoidal signals propagates toward the positive $\theta$ direction in case that the sinusoidal wave $u_A$ leads $u_B$ by 90° phase difference. However, an initial part wave remains in front of the destructive interference and propagates toward the negative $\theta$ direction. In case that wave B leads wave A by 90°, a similar interference can be observed, but travels in opposite direction. The WW-USM can bi-directionally operate by applying two mutually orthogonal AC voltages on both transducers at a resonant frequency of specific wedge wave mode.

### 2.3. Modal sensor equation

Piezoelectric ceramics exhibit hexagonal symmetry. Let the polarization direction be parallel to the $x_3$ direction. For a circular cylindrical PZT tube which is poled radially, the piezoelectric constant $e_{31}$ is identical in both circumferential and axial directions. Hence, the charge output of these materials is independent of the direction of the in-plane normal strains. The electric charge induced over the sensor area covering the outer surface of the piezoelectric tube is a function of its deformation. The modal sensor equation reveals the coupling between mechanical deformation and electric output [25].

$$Q_r = \int_A \{\varepsilon_{33}^S E_r + e_{33}S_r + e_{31}(S_\theta + S_z)\}dA \qquad (8)$$

where $e_{33}$ and $e_{31}$ are the piezoelectric constants of the material, $\varepsilon_{33}^S$ the dielectric constant. Both electric charge $Q_r$ and electric field $E_r$ are measured and applied in the radial direction. The surface area $A$ is underlain by the modal sensor electrodes on the PZT tube. The normal strains $S_\theta$ and $S_z$ are measured in the circumferential and axial directions.

## 3. Simulations

### 3.1. Structural design

A WW-USM stator comprises three main components, including a circular wedge, a piezoceramic tube, and a two-segment base. All components were adhered together by epoxy. The influence from epoxy was ignored hereafter in calculations. The stator base and circular wedge were made of stainless steel (mass density $\rho = 7.82$ g/cm³, Young's modulus $E = 201.25$ GPa, Poisson ratio
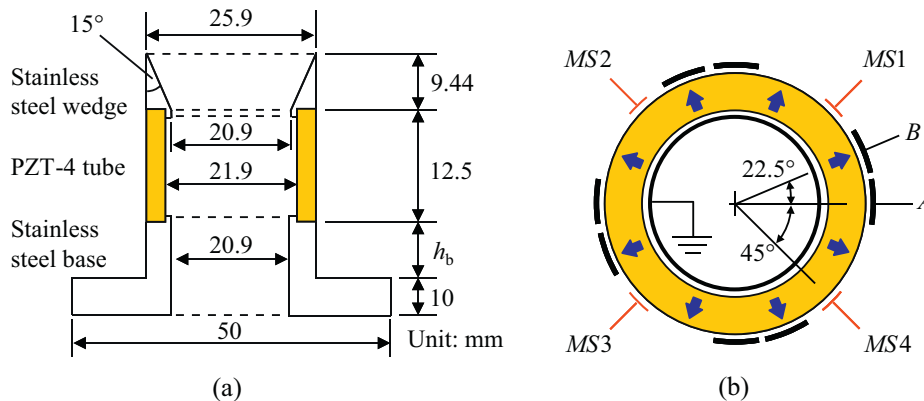


**Fig. 4.** The structure of a WW-USM stator: (a) sectional view and (b) top view of the dual phase electrodes and integrated modal sensors.
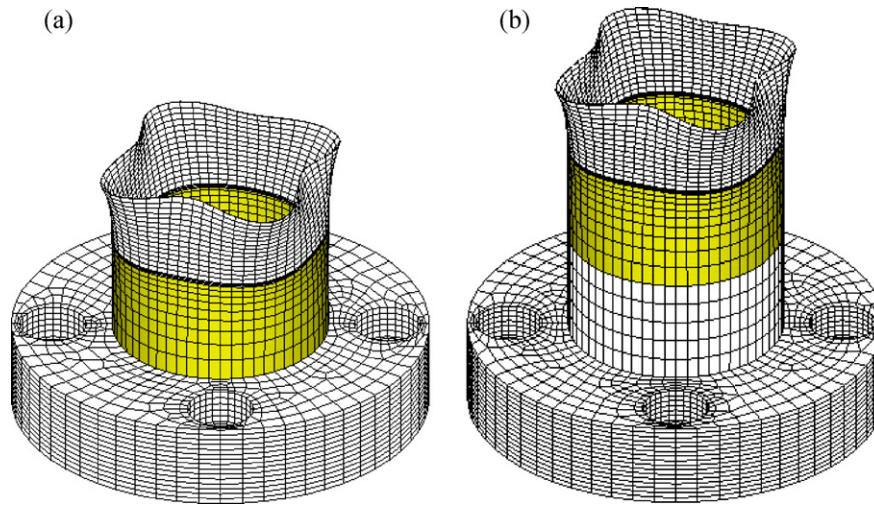
(a)    (b)



**Fig. 5.** Mesh view of the resonant flexural mode $F(1, 4)$ of the WW-USM stator with an upper base height of (a) $h = 0$ and (b) $h_b = 12.5$ mm.

$\nu = 0.29$). The rotors were made of Navy brass ($\rho = 8.47$ g/cm$^3$, $E = 105.46$ GPa, $\nu = 0.34$). The piezoceramic tube was polarized in radial direction. The charge coefficients used in numerical calculation were $d_{33} = 289$ pC/N, $d_{31} = -123$ pC/N. A sectional view of the WW-USM stator is shown in Fig. 4(a). A cylindrical Navy brass rotor contacts the inclined surface of the stainless steel wedge. The latter is attached to the top of a PZT tube. The PZT tube was mounted on a stiff stainless steel base to provide thrust to the rotor. The PZT tube has an inner diameter of 21.9 mm, outer diameter 25.9 mm, and height of 12.5 mm.

The electrodes and modal sensor stripes were parallel to the longitudinal axis placed on the outer surface of PZT tube by screen printing technique. The inner surface was printed with full electrode. This process requires 10 min of heating in a furnace at 120 °C. Fig. 4(b) shows the top view of the dual-phase electrodes A, B and the integrated modal sensors (MS). Both electrodes were exerted by two 90° out-of-phase AC voltages. In the current prototype, the wedge has an apex angle of 15° and a height of 9.44 mm. There remained a 40 μm truncation on the wedge apex due to machining tolerance.

As mentioned earlier, the ANSYS code was used for numerical analysis in this study. We adopted the eight-node coupled-field hexahedral element SOLID5 to approximate the circular cylindrical WW-USM. As examples, the motor stators of $h_b = 0$ and 12.5 mm were modeled by 60,440 elements with 73,200 nodes, and 80,440 elements with 89,200 nodes, respectively. In both cases, there were 1244 fully fixed nodes on the bottom of the stepped base. Fig. 5 shows a mesh view of the resonant mode $F(1, 4)$ for a circular wedge-like stator with different upper base heights. The largest deformation apparently happened at the wedge apex. Hence, the highest particle velocity occurs at the apex.

### 3.2. Vibration analysis

Vibrations of the circular cylindrical structure are classified into three categories: longitudinal modes, torsional modes, and flexural modes. The longitudinal modes and torsional modes are axisymmetric modes, but the flexural modes are not. The latter have three mutual orthogonal motion components. The flexural vibration modes of the clamped-free hollow cylinders are usually labeled by $F(m, n)$. The first integer $m$ denotes the number for a vibration mode with $m$ zero-displacement nodes along the axial length of a cylinder. The second integer $n$ represents the circumferential mode number, which refers to the number of wavelengths in the standing wave around the circumference. Modes for which $n = 1$ are called

beam modes, while the remaining flexural modes are called circumferential modes. The resonant frequencies are functions of the dimensions of the stator. As an example, changing the height of upper stepped base can effectively adjust the modal density.

### 3.3. Modal separation

The fundamental resonant frequency of commercial piezoelectric products is one of the important material properties supplied by most manufacturers. However, these products might not be satisfactory for a clear modal separation in the neighborhood of the driving frequency of USM. Additionally, resonant frequencies do not monotonically appear in the order of resonant vibration modes. Therefore, trimming modal separation between resonant frequencies is essential in designing a WW-USM. Changing the height $h_b$ of the upper stepped base significantly affects modal separation. This study presents an approach for trimming modal separation using ANSYS code.

Resonant frequencies decrease as the value of $h_b$ increases, especially for the axial mode number $m \geq 2$, as shown in Fig. 6. In this figure, the double circle indicates the resonant frequency of $F(1, 4)$ mode was 36.950 kHz and the $F(2, 2)$ mode was 36.627 kHz. The frequency difference between the $F(1, 4)$ and $F(2, 2)$ modes is only 323 Hz when $h_b = 0$. It is easy to stimulate both modes simultaneously, and inducing unexpected disturbance at the instant of switching on/off or changing the direction of the motor. The three single circles in Fig. 6 represent the resonant frequency of $F(1, 4)$ mode occurring at 36.617 kHz, the $F(2, 2)$ mode at 23.815 kHz, and the $F(2, 1)$ mode at 31.544 kHz when $h_b = 12.5$ mm. The resonant frequency of the $F(2, 2)$ mode decreases 12.812 kHz in case that $h_b$ increases from 0 to 12.5 mm. Table 1 lists the changes in resonant frequencies of the stator obtained by the ANSYS code if the upper stepped base height $h_b$ increases from 0 to 12.5 mm. Selecting

**Table 1**
Calculated resonant frequencies of the WW-USM for an upper base height of $h_b = 12.5$ mm. The values in parentheses are those for $h_b = 0$.

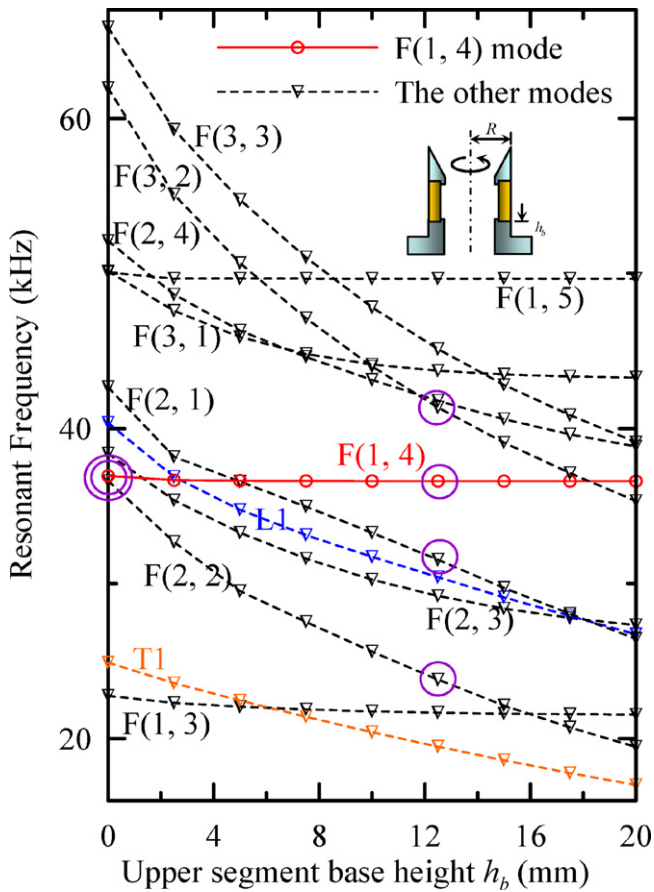| $n$ | Resonant frequency (kHz) | | |
|---|---|---|---|
| | $m = 1$ | $m = 2$ | $m = 3$ |
| 1 | 11.063 (16.676) | 31.544 (42.665) | 41.792 (52.100) |
| 2 | 9.859 (13.252) | 23.815 (36.627) | 41.358 (61.964) |
| 3 | 21.679 (22.770) | 29.207 (38.383) | 45.127 (65.867) |
| 4 | 36.617 (36.950) | 43.726 (52.149) | 58.811 (74.954) |
| 5 | 49.667 (50.066) | 64.006 (68.873) | 79.979 (90.683) |

**Fig. 6.** Plot of calculated resonant frequencies vs. upper base height $h_b$ (F: flexural mode, T: torsional mode, and L: longitudinal mode).

$h_b$ = 12.5 mm as the height of upper stator base and the resonant frequency of flexural mode $F(1, 4)$ to drive the WW-USM could achieve excellent modal separation from the nearest neighboring modes $F(2, 1)$ or $F(4, 2)$. The frequency difference between the modes $F(1, 4)$ and its very next resonant modes was at least 5 kHz.

### 3.4. Harmonic analysis

The harmonic analysis was carried out to analyze the dynamic response of the WW-USM in a steady state. The stator was assumed to have a slight attenuation with a damping factor $\zeta$ = 0.2%. The dual-phase AC voltages of amplitude 400 $V_{pp}$ and frequency 36.617 kHz were applied to the electrodes. Material attenuation could alter the magnitude and phase of particle motion. In case that particle motion has different magnitude or nonlinear phase angle around the circumference of the wedge, wobble motion will induce during operation. Fig. 7 shows the amplitude and phase of circumferential displacement $U_\theta$ over the inclined surface of the wedge at section $\theta = 0°$ when $h_b$ = 12.5 mm. The solid circles with integer numbers (1–6) indicate the contact positions between the stator and the rotor. The circumferential displacement $U_\theta$ has a variation in amplitude and phase over the inclined surface of the wedge. The maximum values in both amplitude and phase occur at position #1, which is about 1.26 mm below the wedge apex. The minimum phase of the circumferential displacement $U_\theta$ occurs at position #6, approximately 8.18 mm below the apex.

Fig. 8 reveals the amplitude and phase distributions of the circumferential displacement $U_\theta$ vs. wedge circumferential angle ($-180° \leq \theta \leq 180°$) at distinct positions on the inclined surface (#1, #3, and #6 in Fig. 7). The phases shown in this figure are linear and
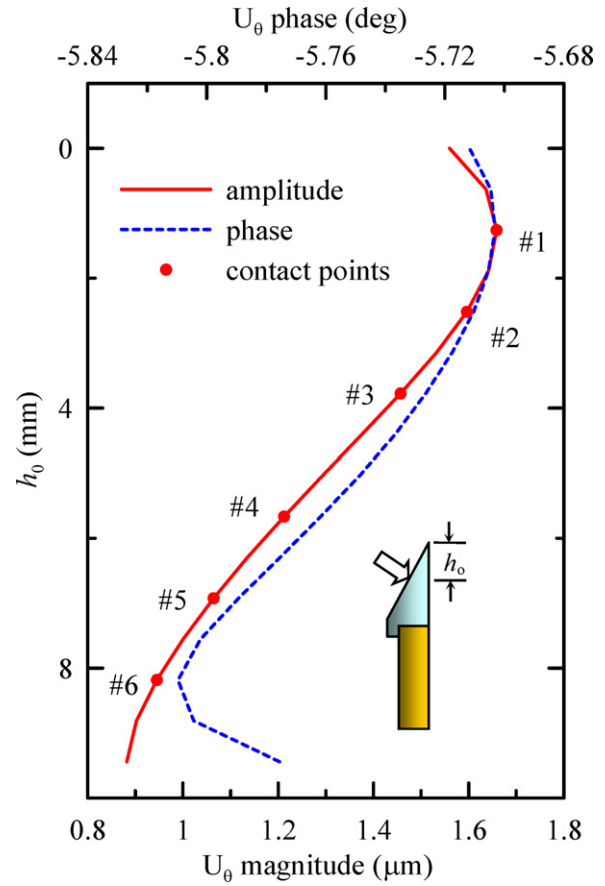


**Fig. 7.** Amplitude (solid line) and phase (dashed line) of the calculated circumferential displacement $U_\theta$ of flexural mode $F(1, 4)$ on the wedge inclined surface as $h_b$ = 12.5 mm.



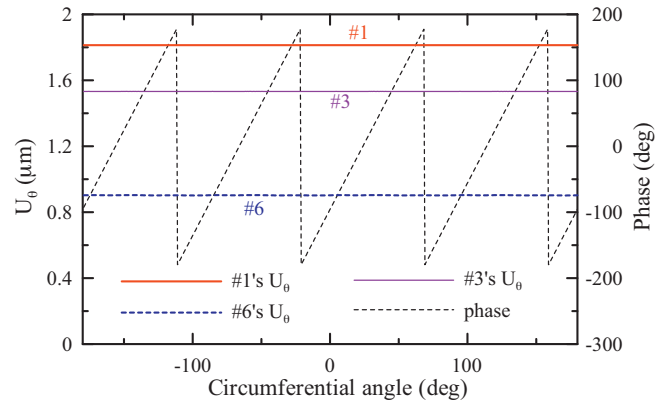**Fig. 8.** Calculated amplitudes and phases of constructed wedge wave motion around the wedge circumference ($-180° \leq \theta \leq 180°$).

independent of the axial positions. Numerical simulation demonstrates that the constructed wedge wave propagates in a constant phase velocity around the circumference. However, the magnitudes exhibit minimal fluctuation along the wedge circumference with a deviation less than 0.14%.

### 3.5. Transient responses

Transient response of a USM at the instant of altering driving voltages depends on the natural vibration characteristics of motor and has mechanical influence on precision motion control. The transient response of the WW-USM stator was numerically
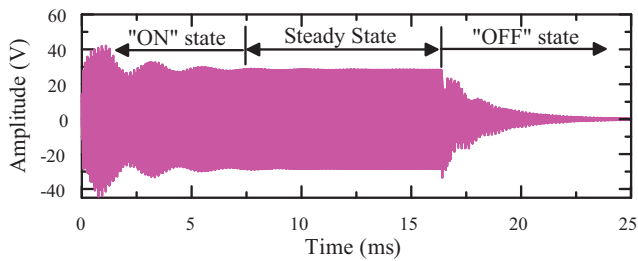
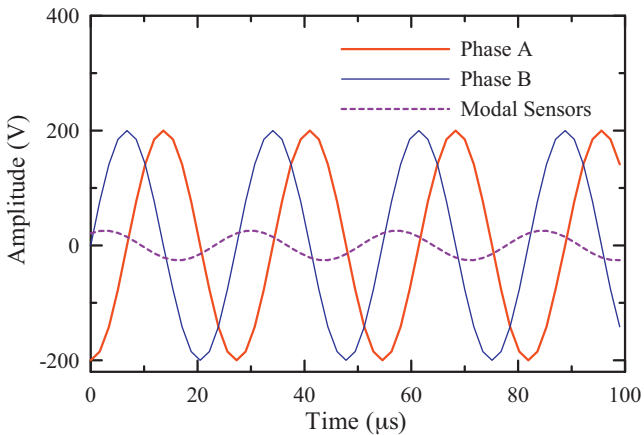**Fig. 9.** Calculated transient response detected by modal sensors.



**Fig. 10.** AC driving voltages and simulated signal recorded by modal sensors in a steady state.



**Fig. 11.** Photo of the stator and three rotors of the prototype WW-USM.

The piezoceramic tube made of PZT-4 was supplied by Eleceram Inc. (Taiwan). A small mistake in the fabrication process can cause motor rotation to be unstable, or create the deviation in the resonance frequency between the simulation and the experiment. For example, if the PZT tube and the stainless steel base are not adhered tightly, that would cause the wave distortion and prevent the traveling wave from concentrating at the wedge tip. This in turn would render the rotor unable to operate. The photos of the WW-USM stator, rotors and the performance test fixture are demonstrated in Figs. 11 and 12, respectively.

This study measured the frequency response function of impedance and its phase, as shown in Fig. 13, through a parallel connection using an HP 8751 network analyzer (Agilent Technologies, Santa Clara, CA, USA). The red dashed line indicates the impedance curve of load-free WW-USM, while the red solid line indicates the

simulated using the implicit Newmark integration provided in the ANSYS code. Assume that the system is initially at rest and in static equilibrium. The proportional damping constants of the stator are assumed to be $\alpha = 485$ rad/s and $\beta = 8.4 \times 10^{-9}$ s/rad, in the case that the damping factor $\zeta$ is 0.2% at the resonant frequency of $F(1, 4)$. Adopt the resonant frequency $f_r = 36.008$ kHz as the driving frequency $f_d$, and apply AC voltages $V_A(t) = 200 \sin(\omega_d t)$ and $V_B(t) = 200 \cos(\omega_d t)$ to both electrodes, respectively.

Fig. 9 shows the calculated transient response detected by four parallel connected modal sensors. In simulation, excitation was immediately turned off after 600 cycles, approximately 16.663 ms after the starting time. The amplitude of the response exhibits that residual vibration exponentially decayed after 600 cycles. Oscillation terminated after 1000 cycles. The envelope response voltage exhibited a beating phenomenon until reaching the steady state. The response of the stator from power on to off can be divided into three stages: the "ON" state, steady state, and the "OFF" state. The setting time, defined as the time required for the vibration to reach and stay with ±1% of the steady-state value, was 7.51 ms. The peak amplitude occurred at 0.96 ms, and the maximum percent overshoot was 36%. Fig. 10 shows the dual phase sinusoidal voltages applied on the electrodes and the calculated signal detected by modal sensors in the steady state. Provided that amplitudes of the mutually orthogonal driving voltages are 400 V$_{pp}$, the estimated output voltage is about 25.46 V$_{pp}$.

## 4. Experiments

### 4.1. Experimental description

The stainless steel wedge, the Navy brass rotors, and stainless steel base were manufactured by lathe processing. The rotor border was embossed with teeth-like structures on the contact points to increase the friction force between the rotor and the stator.
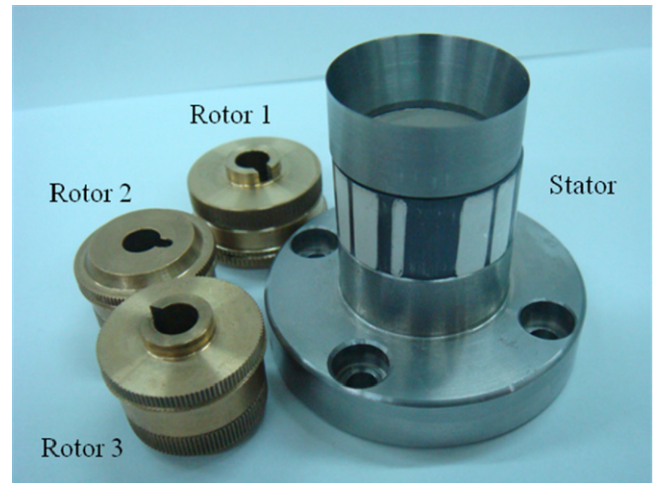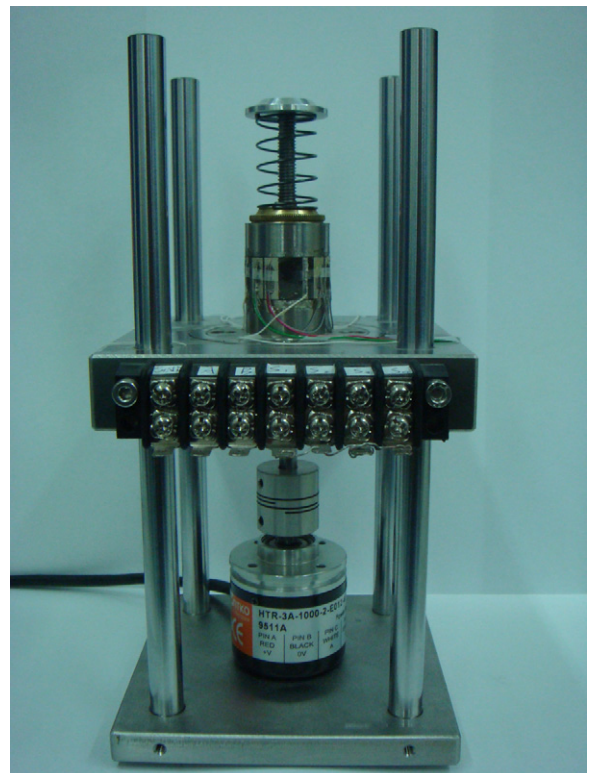


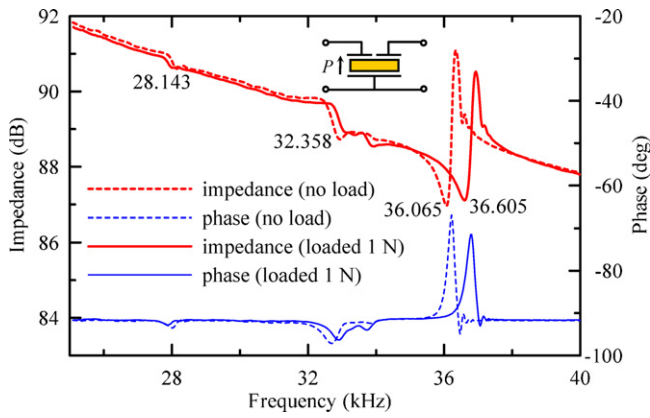**Fig. 12.** Photo of the performance test fixture for WW-USM.

**Fig. 13.** Impedance curve of the WW-USM measured by HP8751. Arrow *P* denotes the poling direction. (For interpretation of the references to color in the text, the reader is referred to the web version of the article.)

impedance curve of WW-USM subjected to 1 N axial preload. The resonant frequency of mode $F(1, 4)$ appears at 36.065 kHz (free) and at 36.605 kHz (1 N axial preload). There remained a 3.7 kHz frequency apart from the nearest neighboring modes. The experimental results slightly drift from the estimated resonant frequency due to assemblage or varying mechanical clamping conditions of the stator.

### 4.2. Modal sensing

The resonant frequencies of small structures are usually measured using non-contact optical interferometers, e.g., laser Doppler vibrometer (LDV), to get rid of the influence of the added mass of the installed accelerometer. However, it is still of difficulty to correlate the measured resonant frequencies with their corresponding vibration modes. This study measured the resonant frequencies and dynamic response of the WW-USM during operation using the modal sensors designed for the desired flexural mode $F(1, 4)$.
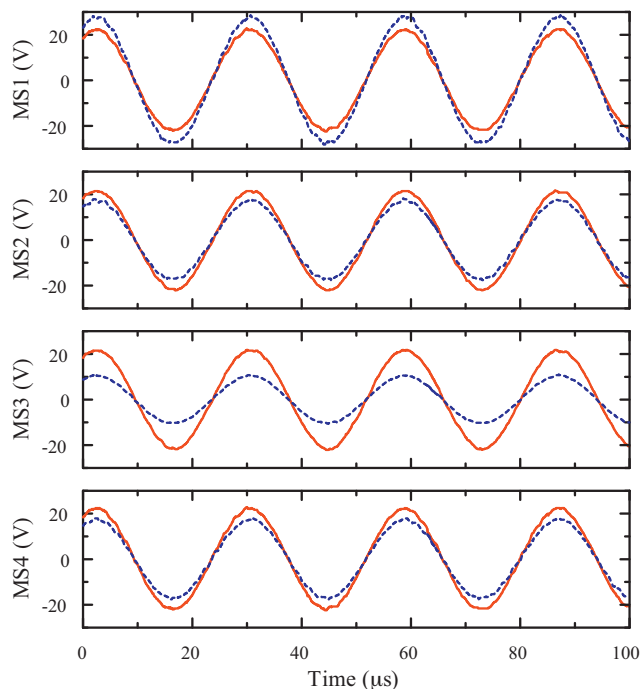


**Fig. 14.** Proper signals (solid lines) and improper signals (dashed lines) detected by four modal sensors.
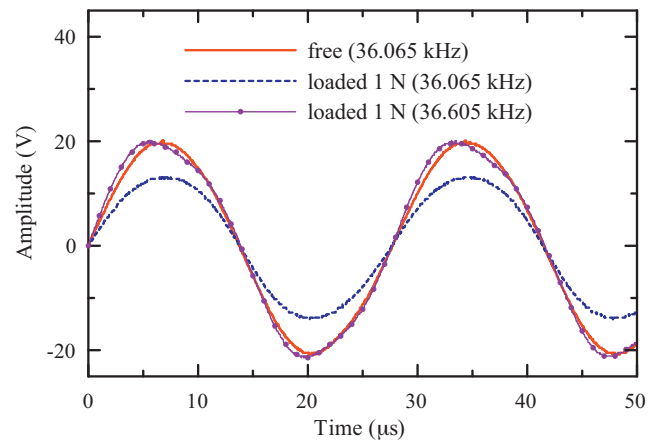


**Fig. 15.** Free and loaded transient responses detected by modal sensors.

Four electrodes were placed on the outer surface of the PZT tube at an equal angular space interval together with the full-circle electrode on the inner surface to form the modal sensors. The electric charge over both inner and outer electrode coverage areas is proportional to the strains generated by the wedge waves around the stator circumference. A time-dependent electrical signal was then induced in a closed circuit of a modal sensor. The largest response of mode $F(1, 4)$ was obtained in case that the maximum amplitude of dynamic strains passed over the sensors. This placement of modal sensors may detect other resonant responses, but they are less distinct than that of $F(1, 4)$ mode. The modal sensors can help tune the driving frequency of WW-USM during operation, and monitor the performance of the constructed traveling wave propagating in the stator. The traveling wave cannot be constructed if the driving frequency significantly differs from the desired resonant frequency or corresponds to other resonant modes.

A typical example is shown in Fig. 14, in which the proper and improper signals were measured by the modal sensors. The proper signals detected by the modal sensors were of the same amplitude and phase. The improper signals were produced by a flexural mode in different electrode layout other than the excitation for $F(1,4)$. The amplitude of improper signal captured by MS1 was relatively large, and the signal amplitude of MS3 was smaller than the proper. Although the amplitudes observed by each sensor may not be the same, their phases are identical. Fig. 15 illustrates the signals of the traveling waves induced at different driving frequencies or under distinct loading conditions. The resonant frequencies drift in case of different preload exerted on the test object. Under the same driving frequency, different preloads might yield decreasing amplitude. A satisfactory time-harmonic signal appeared, but phase shifted, if the traveling wave was driven at the resonant frequency, $f_r = 36.605$ kHz, of the same mode $F(1, 4)$ under 1 N preload.

A pair of 600 cycle burst signals of amplitude 400 $V_{pp}$ with 90° phase difference were applied to the electrodes A and B to drive the USM. Fig. 16 shows the actual transient wave motion detected
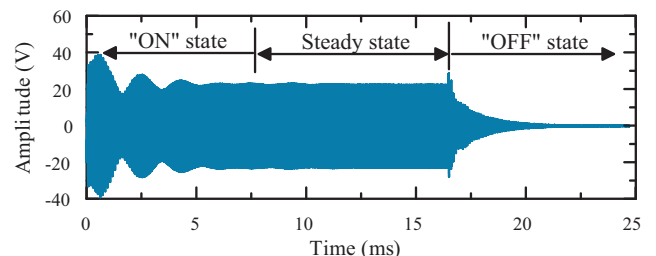


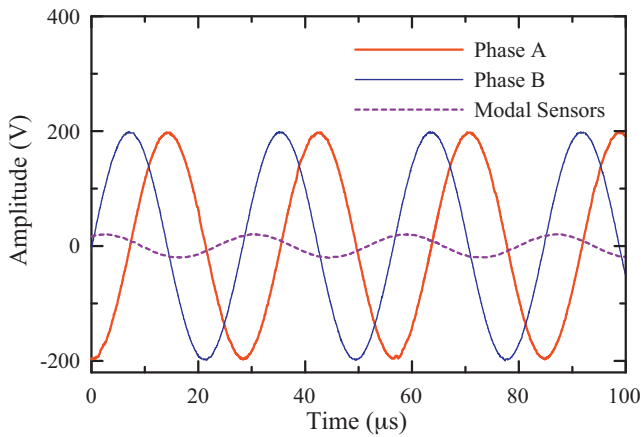**Fig. 16.** Actual transient response detected by the modal sensors.

**Fig. 17.** Actual AC driving voltages and signal detected by modal sensors in a steady state.



**Fig. 19.** Curves of angular speed vs. driving voltage of the WW-USM under a preload of 1 N.

by parallel connected modal sensors. The setting time was 7.65 ms, and the peak amplitude happened at 0.88 ms. The maximum percent overshoot was 45%. The beating phenomenon was found in the amplitude of the response which exponentially decayed after 600 cycles, approximately 16.391 ms after the starting time. Oscillation ceased after 1000 cycles. Compared with the calculated results shown in Fig. 9, the damping ratio $\zeta$ in the real motor might be higher than the estimated value 0.2%. Fig. 17 shows the dual-phase sinusoidal driving voltages and real signal measured by modal sensors in the steady state.

### 4.3. Performance test

Fig. 18 demonstrates the schematic diagram of the performance test setup for the prototype WW-USM. A phase shifter was used to split the signal produced by the function generator into two mutually orthogonal sinusoidal driving voltages. The amplitudes of both dual phase signals were gained to drive the motor by two power amplifiers A-303 (A.A. Lab Systems Ltd., Israel). The transient response of the stator was detected by modal sensors connected in parallel and captured by a digital oscilloscope LeCroy WS42Xs (LeCroy Corp., New York, USA). An encoder HRT-3A (1000 ppr, Hontko Inc., Taiwan) recorded the angular speed of the WW-USM. The output torque of the WW-USM was measured using a simple setup,
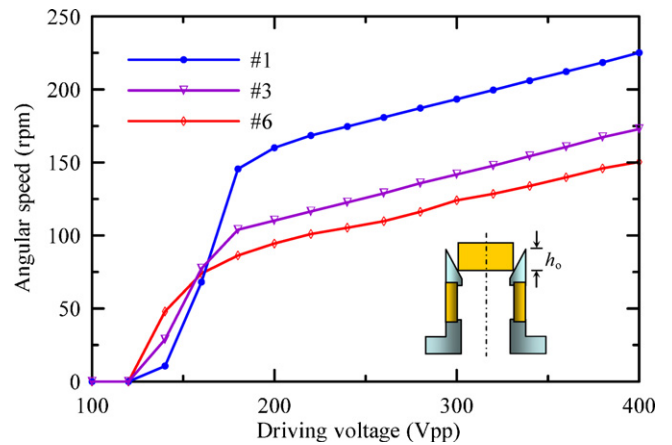
in which a steel wire embracing the rotor hung a weight at one end, and connected to a load cell FUTEK LSM400 (Futek Advanced Sensor Technology, Inc., CA, USA) at the other end. The load cell signal was magnified by a low-noise conditioning amplifier Vishay 2210B (Vishay Micro-Measurement, Inc., Munich, Germany) and recorded by the NI-PXI-DAQ 6251 data-acquisition module (National Instrument Corp., TX, USA).

Measure the angular speed when the motor was subjected to 1 N axial preload and driven at frequency of 36.605 kHz. Fig. 19 shows that the angular speed of the rotor was proportional to the amplitude of driving voltage, and the threshold voltage was approximately 110–130 $V_{pp}$. The angular speed is also a function of the contact position between the rotor and stator. Six contact points were considered for comparison. The distance measured from the contact position to the wedge apex $h_0$ is 1.26, 2.52, 3.79, 5.66, 6.92, and 8.18 mm, respectively. The contact points are numbered as #1 to #6. The shorter distance the contact position is apart from the wedge apex, the faster the revolution speed. As examples, the angular speeds are 225, 173, and 150 rpm for driving voltage of 400 $V_{pp}$ while the contact positions located at points #1, #3, and #6.

The angular speed vs. output torque curves for the contact positions located at points #1, #3, and #6 are shown in Fig. 20(a). The maximum output torque was 15.736 mN m when the contact
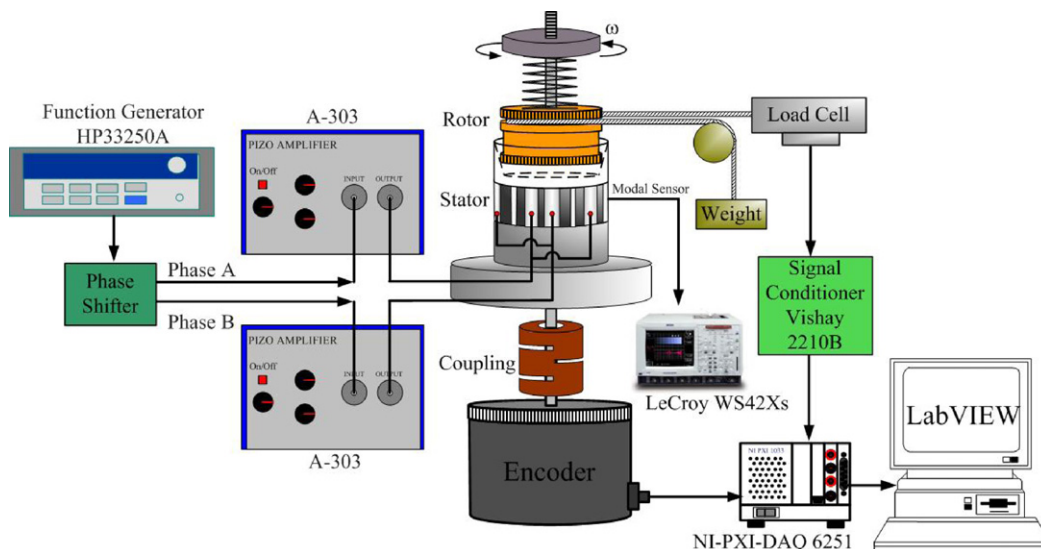


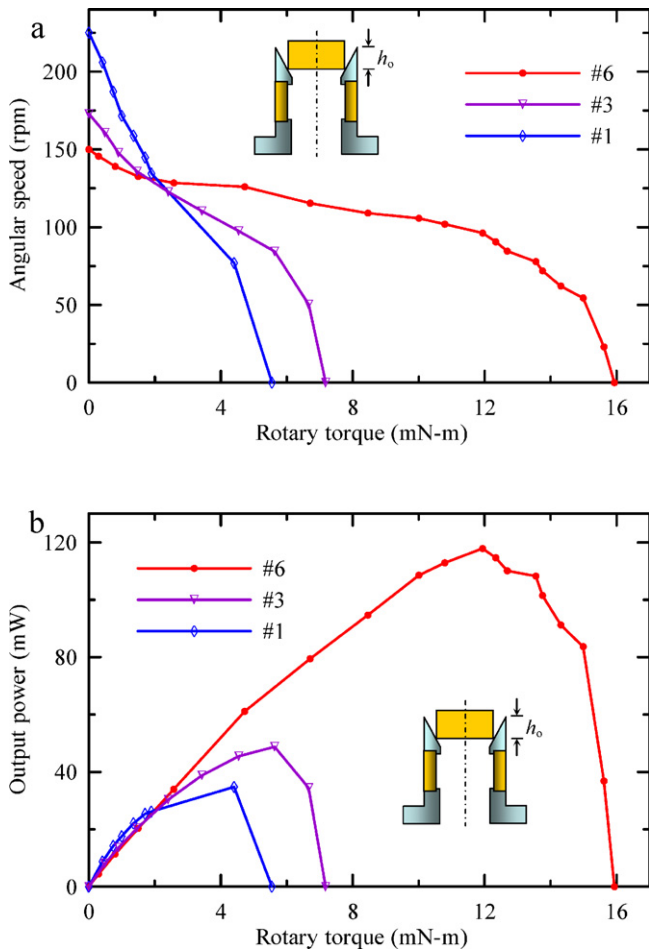**Fig. 18.** Experimental setup for the test of WW-USM.

**Fig. 20.** Performance curves of a WW-USM prototype under a preload of 1 N at various contact positions: (a) curves of angular speed vs. rotary torque and (b) curves of output power vs. rotary torque.

position located at the point #6. Fig. 20(b) demonstrates the output power vs. rotary torque at three contact positions (#1, #3, and #6). The WW-USM produced relatively high power while the contact position was located at a lower point. Fig. 21 shows both the maximum angular speed and output torque measured at every contact point. The intersection of both curves provides a compromise between angular speed and output torque. However, only moderate mechanical power could be delivered. Fig. 22 reveals a cross-sectional view of the stainless steel wedge with the
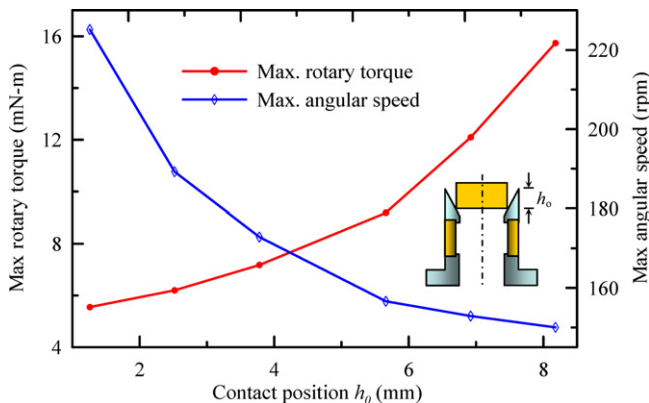


**Fig. 21.** The maximum angular speed and the maximum output torque at different contact positions. The contact position is measured from the wedge apex.
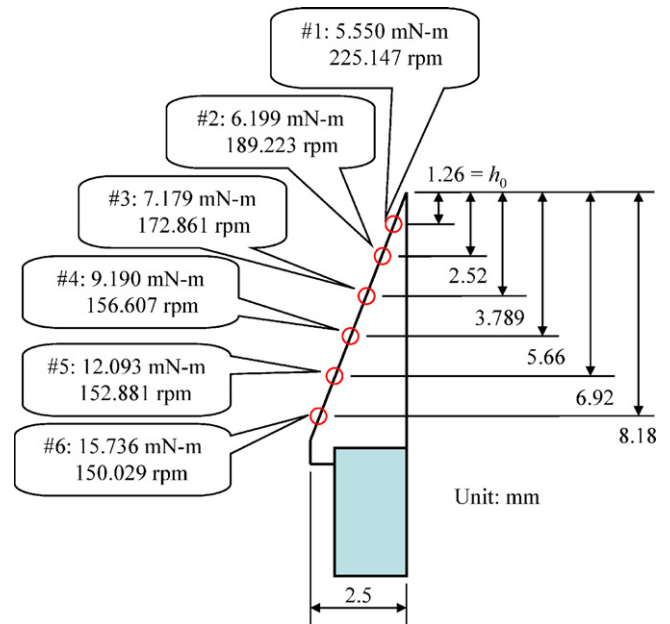


**Fig. 22.** The maximum angular speeds and output torques in case of the rotor in contact with the inclined surface of the wedge stator at different positions.

maximum output torque and angular speed measured for different contact positions on the wedge inclined surface. The maximum mechanical power was 120 mW and the maximum electromechanical transduction efficiency was 16.22%.

## 5. Discussion

The exact solution of acoustic waves in either linear or circular elastic wedges has not been available yet. We used finite element method to design and analyze the wedge-like stator for the rotary WW-USM. In this work, the natural modes, resonant frequencies, time-harmonic and transient responses of the wedge waves in stators were calculated through the commercial code ANSYS. The proposed WW-USM is driven by a traveling wedge wave and the friction forces between the rotor and the stator. The motor stator comprises a circular stainless steel wedge, PZT-4 tube, and a stainless steel base. Due to anisotropic sintering contraction, the commercial PZT tube products could not directly satisfy our design requirements. This study considered a two-segment base, in which the upper base height was determined in accordance with a better modal separation near the specific driving mode. The fundamental flexural mode $F(1, 4)$ was selected to drive the motor. Its resonance had been tuned to occur near 36.617 kHz with at least 3.7 kHz separation apart from the nearest neighboring modes.

Large flexural deformation appears at the wedge apex and its vicinity. Hence, the WW-USM reached the maximum angular speed in case that the contact position between the rotor and stator was located near the apex. However, the stiffness near the apex is too weak to provide the force needed to thrust the rotor. In contrast, the small deformation in the base region of the wedge indicates it has more stiffness to exert thrust on the rotor. According to the experimental results, the proposed WW-USM can exchange the angular speed for torque output. A flexible mechanical performance only depends on the contact position of the rotor on the inclined surface of the wedge stator.

Both simulation and experimental results agree well. This study ensures that the proposed motor functions as anticipated. The concept of modal sensors was successfully realized to detect the quality of traveling waves. Various operating demands, including payload, wear, angular speed, and output torque, would alter
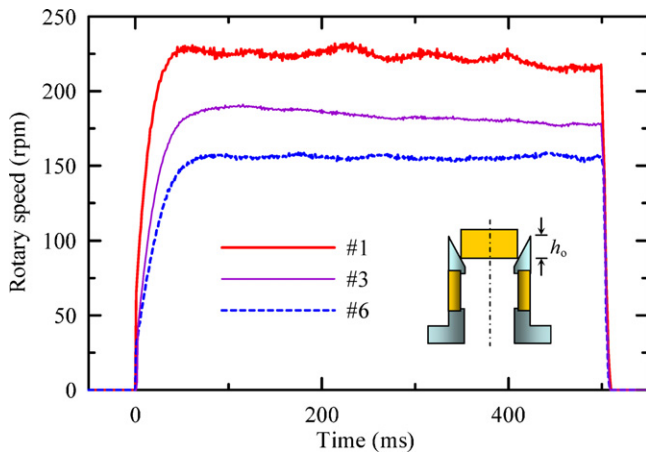
**Fig. 23.** Transient angular velocity of the prototype WW-USM.

the driving conditions. The influence of driving conditions such as amplitude, driving frequency, phase difference, and preload can be detected for feedback control to achieve the optimal performance of WW-USM. The modal sensors were first used to monitor dynamic response of the WW-USM instead of other expensive optical instruments. It is found that the amplitude of detected signal decreased if the rotor exerted a payload or preload on the stator. Once the driving frequency was adjusted and fitted the resonant frequency of the loaded system, the signal amplitude increased. Modal sensors can detect the rotary direction of the rotor and estimate the angular speed of the rotor. The transient angular velocity recorded at three contact positions (#1, #3, and #6) are shown in Fig. 23.

Finally, this study analyzed the transient response of WW-USM. The operating period can be divided into three stages, including the "ON" state, steady state, and "OFF" state, from start to stop. Most of the earlier researches focused on the "ON" state right after power on and the subsequent steady state. Few studies discussed the "OFF" state. Although residual waves still propagate around the wedge in the "OFF" state, the energy of the remaining wave becomes evanescent due to the friction between the rotor and stator. Therefore, the rotor would stop rotation immediately.

## 6. Conclusions

This study develops a new WW-USM driven by circumferential modes rather than the beam mode used in a conventional cylindrical USM. Simulation and experimental results indicate that the proposed prototype motor operates as expected. The proposed design prevents abnormal wobbling of the rotor and stress concentration. Adjusting the driving voltage and specific phase difference between the two comb transducers makes it feasible to control the angular speed and rotation direction.

According to the comparison of maximum angular speed and torque of the motor measured at different contact positions (Fig. 22), the revolution speed of the motor decreases with increasing distance from the apex to the contact position. In contrast, the output torque increases with increasing distance between both. These results reveal a trade off between output torque and angular speed by varying the contact position between the rotor and the stator without a need to modify the entire structure. The proposed motor has a flexible mechanical performance for some applications required priority of angular speed or output torque. Moreover, using the modal sensors to real time monitor the transient response quality has achieved good results. The self-sensing mechanism has been verified. Although the output torque of the prototype WW-USM is still small, an excess torque output can be

achieved by increasing the preload and driving voltage. A large aspect ratio WW-USM, in which the radius is relatively larger than the height of the wedge, can magnify the output torque in case of the same thrust exerted on the contact surface. Reducing power consumption and enhancing the overall performance of the WW-USM requires adding an appropriate frictional material between the rotor and the stator.

## Acknowledgments

## References

[1] T. Sashida, T. Kenjo, An Introduction to Ultrasonic Motors, Clarendon, Oxford, 1993.
[2] M. Kurosawa, S. Ueha, Hybrid transducer type ultrasonic motor, IEEE Trans. Ultrason. Ferroelectr. Freq. Control 38 (1991) 89–92.
[3] P. Hagedorn, J. Wallaschek, Travelling wave ultrasonic motors. Part I: working principle and mathematical modelling of the stator, J. Sound Vib. 155 (1992) 31–46.
[4] P. Hagedorn, J. Wallaschek, W. Konrad, Travelling wave ultrasonic motors. Part II: a numerical method for the flexural vibrations of the stator, J. Sound Vib. 168 (1993) 115–122.
[5] M. Aoyagi, Y. Tomikawa, T. Takano, Ultrasonic motors using longitudinal and bending multimode vibrators with mode coupling by externally additional asymmetry or internal nonlinearity, Jpn. J. Appl. Phys. 51 (1992) 3077–3080.
[6] T. Morita, M. Kurosawa, T. Higuchi, Cylindrical micro ultrasonic motor using PZT thin film deposited by single process hydrothermal method, IEEE Trans. Ultrason. Ferroelectr. Freq. Control 45 (1998) 1178–1187.
[7] F. Lu, H.P. Lee, S.P. Lim, Modeling of contact with projections on rotor surfaces for ultrasonic traveling wave motors, Smart Mater. Struct. 10 (2001) 860–866.
[8] B. Koc, S. Cagatay, K. Uchino, A piezoelectric motor using two orthogonal bending modes of a hollow cylinder, IEEE Trans. Ultrason. Ferroelectr. Freq. Control 49 (2002) 495–500.
[9] D. Sun, J. Lin, X. Ai, Modeling and performance evaluation of traveling-wave piezoelectric ultrasonic motors with analytical method, Sens. Actuators A: Phys. 100 (1) (2002) 84–93.
[10] X. Xu, Y.C. Liang, H.P. Lee, W.Z. Lin, S.P. Lim, K.H. Lee, X.H. Shi, Mechanical modeling of longitudinal oscillation ultrasonic motors and temperature effect analysis, Smart Mater. Struct. 12 (2003) 514–523.
[11] M. Tominaga, R. Kaminaga, J.R. Friend, K. Nakamura, S. Ueha, An ultrasonic linear motor using ridge-mode traveling waves, IEEE Trans. Ultrason. Ferroelectr. Freq. Control 52 (2005) 1735–1742.
[12] O. Vyshnevskyy, S. Kovalev, J. Mehner, Coupled tangential-axial resonant modes of piezoelectric hollow cylinders and their application in ultrasonic motors, IEEE Trans. Ultrason. Ferroelectr. Freq. Control 52 (2005) 31–36.
[13] A. Iula, M. Pappalardo, A high-power traveling wave ultrasonic motor, IEEE Trans. Ultrason. Ferroelectr. Freq. Control 53 (2006) 1344–1351.
[14] Y. Ma, C. Pan, Q. Zhang, F. Kong, Z. Feng, Two-phase piezoelectric motor using a multiple-tube structure actuator, Jpn. J. Appl. Phys. 48 (2009) 096501.
[15] D. Sun, S. Wang, J. Sakurai, K.B. Choi, A. Shimokohbe, S. Hata, A piezoelectric linear ultrasonic motor with the structure of a circular cylindrical stator and slider, Smart Mater. Struct. 19 (2010) 045008.
[16] P.E. Lagasse, Analysis of a dispersion free guide for elastic waves, Electron. Lett. 8 (1972) 372–373.
[17] V.V. Krylov, Geometrical-acoustics approach to the description of localized vibrational modes of an elastic solid wedge, Sov. Phys. Tech. Phys. 35 (2) (1990) 137–140.
[18] V.V. Krylov, Localized vibration modes propagating along edges of cylindrical and conical wedge-like structures, J. Sound Vib. 227 (1) (1999) 215–221.
[19] A.C. Hladky-Hennion, Finite analysis of the propagation of acoustic wave in waveguides, J. Sound Vib. 194 (1996) 119–136.
[20] V.V. Krylov, Propagation of wedge acoustic waves along wedges embedded in water, in: Proc. IEEE Ultrason. Symp., Cannes, France, 1994, pp. 793–796.
[21] V.V. Krylov, G.V. Pritchard, Experimental confirmation of the propulsion of marine vessels employing guided flexural waves in attached elastic fins, J. Fluids Struct. 23 (2007) 297–307.
[22] V.V. Krylov, G.V. Pritchard, Experimental investigation of the aquatic propulsion caused by localized flexural wave propagation in immersed wedges and plates, Appl. Acoustics 68 (2007) 97–113.
[23] C.-C. Yin, T.-H. Yu, An ultrasonic motor driven by traveling cylindrical wedge waves, in: 2006 IEEE Ultrasonic Symposium, Vancouver, Canada, October, 2006, pp. 156–159.

[24] T.-H. Yu, S.-Y. Yang, C.-L. Lee, C.-C. Yin, Bi-dimensional finite element analysis for modal separation of a circular cylindrical WW-USM, Finite Elements Anal. Des. 47 (7) (2011) 635–642.
[25] J. Callaham, H. Baruh, Modal sensing of circular cylindrical shells using segmented piezoelectric elements, Smart Mater. Struct. 8 (1999) 125–135.

## Biographies

**Tai-Ho Yu** was born in Tainan, Taiwan, in 1960. He received his B.S. and Master's degree in Automatic Control Engineering from Feng Chia University, Taichung, Taiwan, in 1983 and 1988, respectively. He is currently studying for Ph.D. degree in the Department of Mechanical Engineering at National Chiao Tung University, Hsinchu, Taiwan. He has been an instructor at the Department of Electronic Engineering at National United University, Miaoli, Taiwan, since 1988. His research interests are in ultrasonic motors, driving circuit design and its control theories. He is a member of the IEEE UFFC society.

**Ching-Chung Yin** received his B.Sc. and M.Sc. degrees in Naval Architecture from National Taiwan University, Taipei, Taiwan in 1981 and 1983, respectively. In 1990 he received the Ph.D. degree in Aerospace Engineering from University of California, Los Angeles (UCLA). In 1991, he joined the Department of Mechanical Engineering, National Chiao Tung University, Hsinchu, Taiwan, and is now an associate professor. He serves as a member of the board of the Society for Nondestructive Testing and Certification of Taiwan (2010–2012). His research interests include ultrasonic nondestructive evaluation, photomechanics, acoustic wave sensors, ultrasonic motors, and acoustic manipulation.